

Cite this: *Nanoscale*, 2026, **18**, 13397

# Composition- and structure-tunable CoNiFe hydroxide nanostructures toward enhanced oxygen evolution reaction

Zihan Zhang,<sup>a,b</sup> Xingxin Jiang,<sup>a,b</sup> Nattapol Ma,<sup>c</sup> Jizhen Zhang,<sup>a</sup> Emmanuel Picheau,<sup>a</sup> Nobuyuki Sakai,<sup>a</sup> Takayoshi Sasaki<sup>a</sup> and Renzhi Ma<sup>a,b</sup>

The electrocatalytic performance of transition-metal layered double hydroxides (LDHs) can be substantially enhanced through compositional and structural engineering. Herein, ternary (CoNiFe) hydroxide nanocones featuring mixed tetrahedral ( $T_d$ ) and octahedral ( $O_h$ ) coordination are rationally designed to boost oxygen evolution reaction (OER) activity. Binary CoNi hydroxide nanocones with mixed coordination are first synthesized, among which a Co : Ni ratio of 3 : 1 exhibits optimal performance with an overpotential of 339 mV at 10 mA cm<sup>-2</sup>. Subsequent Fe incorporation followed by a topochemical oxidative intercalation process convert the CoNiFe(II) hydroxides into CoNiFe(III) LDHs while retaining mixed  $T_d/O_h$  coordination. Benefiting from the synergistic effects of multimetal composition and coordination modulation, the resulting Co<sub>3</sub>Ni<sub>1</sub>Fe<sub>1</sub> LDH nanocones achieve a markedly reduced overpotential of 280 mV. Furthermore, exfoliation into monolayer nanosheets leads to a further enhancement in catalytic activity by increasing exposure of accessible active sites, ultimately lowering the overpotential to 267 mV. This study highlights an effective strategy that integrates compositional optimization, coordination engineering, and structural modulation for the development of high-performance LDH electrocatalysts.

Received 20th January 2026,  
Accepted 10th May 2026

DOI: 10.1039/d6nr00271d

rsc.li/nanoscale

## 1. Introduction

Hydrogen is widely regarded as a promising energy carrier owing to its high gravimetric energy density, carbon-free utilization, and broad applicability across energy and industrial sectors.<sup>1–3</sup> Among various hydrogen production routes, electrochemical water splitting is considered a clean and efficient approach.<sup>4–6</sup> Nevertheless, the overall efficiency of water electrolysis is severely constrained by the oxygen evolution reaction (OER) at the anode, which involves a complex four-electron transfer process and high-energy reaction intermediates, resulting in large overpotentials and significant energy losses.<sup>7–9</sup> Although noble-metal-based catalysts such as RuO<sub>2</sub> and IrO<sub>2</sub> exhibit excellent OER activity and are commonly regarded as benchmark materials, their high cost, scarcity, and limited durability hinder widespread practical application, underscoring the need for cost-effective alternatives with comparable performance.<sup>10–12</sup> Consequently, the exploration of

efficient and Earth-abundant OER electrocatalysts is crucial for improving electrolysis efficiency and enabling large-scale hydrogen production.

Catalysts based on Earth-abundant transition metals, especially Fe, Co, Ni, and Mn, have gained increasing attention as promising substitutes for noble metals.<sup>13–17</sup> Among them, layered double hydroxides (LDHs) are especially appealing due to their highly tunable compositions, flexible layered architectures, and intrinsically abundant active sites.<sup>18–20</sup> In particular, Co-based LDHs have demonstrated superior catalytic activity, which is often attributed to their favorable electronic structure and versatile redox chemistry, making them highly effective for the OER.<sup>21–23</sup> Considerable efforts have been devoted to enhancing the catalytic activity of LDHs, among which structural and morphological engineering have emerged as a particularly effective strategy.<sup>24,25</sup> The construction of well-defined nanostructures with controlled geometries, such as nanocones (NCs), enables effective regulation of the surface curvature and spatial distribution of active sites. These nanocone morphologies not only increase the exposed surface area but also facilitate mass transport and electron transfer, while mitigating stacking and aggregation issues commonly associated with layered materials.<sup>26–29</sup> Notably, the NCs belong to the so-called  $\alpha$  phase featuring a unique coexistence of mixed tetrahedral ( $T_d$ ) and octahedral ( $O_h$ ) coordination and can be topochemically transformed into LDHs.<sup>30–32</sup> Compared with conventional

<sup>a</sup>Research Center for Materials Nanoarchitectonics (MANA), National Institute for Materials Science (NIMS), 1-1 Namiki, Tsukuba, Ibaraki 305-0044, Japan.  
E-mail: MA.Renzhi@nims.go.jp

<sup>b</sup>Graduate School of Advanced Science and Engineering, Waseda University, 3-4-1 Okubo, Shinjuku-ku, Tokyo 169-8555, Japan

<sup>c</sup>International Center for Young Scientists (ICYS), National Institute for Materials Science (NIMS), 1-1 Namiki, Tsukuba, Ibaraki 305-0044, Japan

LDHs containing exclusively octahedrally coordinated metal centers, this mixed coordination configuration enriches the diversity of active sites and contributes to improved catalytic performance.<sup>32</sup> In recent years, expanding binary LDHs to ternary or multimetal systems has proven to be an effective strategy for further boosting OER performance.<sup>33–35</sup> The introduction of additional metal species can modulate the local electronic structure through cooperative cation–cation interactions, enabling precise regulation of coordination environments and valence states.<sup>36–39</sup> Notably, Fe incorporation into Co- and Ni-based hydroxides/LDHs has been widely reported to induce electronic redistribution among metal centers, thereby optimizing the adsorption and conversion of oxygenated intermediates and ultimately enhancing OER kinetics.<sup>40–43</sup>

In this work, ternary CoNiFe layered hydroxide NCs with mixed T<sub>d</sub> and O<sub>h</sub> coordination were designed to systematically investigate the synergistic effects of composition, coordination configuration, and morphology on OER performance. Binary CoNi hydroxide NCs with mixed coordination were first synthesized, followed by the incorporation of Fe to develop ternary CoNiFe systems. Subsequently, a topochemical oxidative intercalation process using iodine converted the  $\alpha$ -phase hydroxides into LDHs (LDH<sub>T<sub>d</sub>/O<sub>h</sub></sub>). By systematically comparing binary and ternary compositions, the role of heteroatom incorporation and coordination modulation in governing electrocatalytic behavior was elucidated. Furthermore, the nanocone-derived LDH<sub>T<sub>d</sub>/O<sub>h</sub></sub> was exfoliated into monolayer nanosheets (NSs) to explore the impact of dimensional reduction on OER activity. This study provides a rational framework for tailoring layered hydroxide electrocatalysts through integrated compositional coordination, and structural engineering.

## 2. Experimental section

### 2.1. Synthesis of binary CoNi hydroxide NCs

CoNi hydroxide NCs were obtained through homogeneous precipitation based on our earlier method with slight modifications.<sup>27</sup> Designated amounts of CoCl<sub>2</sub>·6H<sub>2</sub>O, 70 mmol urea, and 25 mmol sodium dodecyl sulfate (SDS) were dissolved in 1000 mL of deaerated water in a three-neck round-bottom flask. A NiCl<sub>2</sub> solution was also prepared and stored in a pressure-equalizing dropping funnel, which was attached to one of the necks. The total amount of metal precursors (CoCl<sub>2</sub>·6H<sub>2</sub>O and NiCl<sub>2</sub>·6H<sub>2</sub>O) was controlled at 10 mmol with varied Co/Ni ratios (4 : 1, 3 : 1, 2 : 1, and 1 : 1). The flask was then heated in an oil bath to 110 °C and kept under a nitrogen atmosphere for reflux. After refluxing for 5 h, the NiCl<sub>2</sub> solution in the funnel was dropped into the flask. The synthesis proceeded for a total of 8 h. Upon completion, the solid products were isolated and washed repeatedly using water and ethanol.

### 2.2. Synthesis of ternary CoNiFe(II) hydroxide NCs

The preparation route for the ternary hydroxide is similar to the procedure developed for the binary system, with the total

amount of metal precursors (CoCl<sub>2</sub>·6H<sub>2</sub>O, NiCl<sub>2</sub>·6H<sub>2</sub>O, and FeCl<sub>2</sub>·4H<sub>2</sub>O) controlled at 10 mmol. CoCl<sub>2</sub>·6H<sub>2</sub>O, urea (70 mmol), and SDS (25 mmol) were dissolved in 1000 mL of deaerated water in a four-neck round-bottom flask. In parallel, aqueous solutions of NiCl<sub>2</sub>·6H<sub>2</sub>O and FeCl<sub>2</sub>·4H<sub>2</sub>O were individually dissolved in 50 mL of water and transferred into separate pressure-equalizing dropping funnels. CoNiFe(II) hydroxide NCs were synthesized with a series of Co : Ni : Fe molar ratios, including 8 : 1 : 1, 7 : 2 : 1, 7 : 2 : 2, 3 : 1 : 1, 7 : 1 : 2, and 6 : 1 : 3. After approximately 1.5 h of refluxing, the FeCl<sub>2</sub> solution was introduced into the flask, followed by the addition of the NiCl<sub>2</sub> solution when the reaction time reached 5 h.

### 2.3. Synthesis and exfoliation of ternary CoNiFe(III) LDH<sub>T<sub>d</sub>/O<sub>h</sub></sub> NCs

The as-prepared NCs were subsequently transformed into LDH<sub>T<sub>d</sub>/O<sub>h</sub></sub> through a topochemical oxidative intercalation process following established protocols.<sup>32,44</sup> In a typical procedure, 0.5 g of the CoNiFe(II) hydroxide NCs was introduced into 100 mL of I<sub>2</sub>/CHCl<sub>3</sub> solution and kept under continuous stirring for about 24 h. After the reaction, the oxidized LDH<sub>T<sub>d</sub>/O<sub>h</sub></sub> products were collected by filtration and thoroughly rinsed with CHCl<sub>3</sub> and ethanol until the filtrate became clear. To exfoliate, 0.04 g of the resulting CoNiFe(III) LDH<sub>T<sub>d</sub>/O<sub>h</sub></sub> powder was dispersed in 100 mL of degassed formamide and subjected to sonication for 2 h. The mixture was centrifuged at 3500 rpm for 30 min to remove any unexfoliated residues, yielding a translucent colloidal suspension.

### 2.4. Electrochemical measurements

OER measurements were carried out using a standard three-electrode setup on a CH Instruments 760E electrochemical workstation (CHI 760E). For working electrode preparation, 5 mg of catalyst was dispersed in 1 mL of a water/ethanol mixture (1 : 1, v/v) containing 10  $\mu$ L of 10 wt% Nafion solution. The suspension was sonicated for 30 min to form a homogeneous ink, after which 4  $\mu$ L was deposited onto a polished glassy carbon electrode (3 mm diameter) and dried at 60 °C. The resulting catalyst loading was approximately 0.23 mg cm<sup>-2</sup>. 1 M KOH was used as the electrolyte, with a Hg/HgO electrode serving as the reference and a Pt wire as the counter electrode. All potentials were calibrated to the reversible hydrogen electrode (RHE) according to the equation:

$$E_{\text{RHE}} \text{ (V)} = E_{\text{Hg/HgO}} \text{ (V)} + 0.059 \text{ pH} + 0.098$$

Cyclic voltammetry (CV) was initially performed at a scan rate of 30 mV s<sup>-1</sup> from 0 to 0.8 V vs. Hg/HgO until stable curves were obtained. Subsequently, linear sweep voltammetry (LSV) was carried out from 0 to 0.8 V vs. Hg/HgO at a scan rate of 5 mV s<sup>-1</sup> with 95% manual *iR*-compensation. All electrochemical measurements were repeated three times, and consistent results were obtained, confirming the reliability of the data. Tafel slopes were derived from the Tafel equation. Electrochemical impedance spectroscopy (EIS) was conducted at 0.62 V vs. Hg/HgO within a frequency range of 0.1 to 10<sup>5</sup> Hz at an amplitude of 5 mV. CV tests were performed between

0.35 and 0.45 V vs. Hg/HgO at various scan rates (20, 40, 60, 80, and 100  $\text{mV s}^{-1}$ ). The slope of the plot of the current density difference ( $\Delta j = j_a - j_c$ ) at the midpoint of the potential window against the scan rates was calculated to be twice the double-layer capacitance ( $C_{dl}$ ), which was used to estimate the electrochemical surface area (ECSA). For the purpose of excluding the improvement by the ECSA, the OER performance was normalized by the ECSA. The ECSA-normalized current density for the as-prepared catalysts was calculated to be:

$$\text{ECSA-normalized current density} = \text{current density} \times C_s / C_{dl}$$

where  $C_s$  is the specific capacitance. In this work, 0.04  $\text{mF cm}^{-2}$  was adopted as the value of  $C_s$  based on previously reported catalysts in alkaline solutions.<sup>45,46</sup>

### 2.5. Materials characterization

Powder X-ray diffraction (XRD) patterns were collected using a Rigaku Ultima IV diffractometer equipped with Cu K $\alpha$  radiation ( $\lambda = 0.15405 \text{ nm}$ ) operating at 40 kV and 40 mA. In-plane XRD measurements of NSs deposited on Si substrates were performed using synchrotron X-ray radiation ( $\lambda = 0.11988(2) \text{ nm}$ ) at the BL-6C beamline of the Photon Factory, High Energy Accelerator Research Organization (KEK). Morphological and elemental analyses were performed by scanning electron microscopy (SEM, JEOL JSM-6010LA) coupled with energy-dispersive X-ray spectroscopy (EDS). Selected area electron diffraction (SAED) patterns as well as transmission electron microscopy (TEM) and high-resolution TEM (HRTEM) images were acquired using a JEOL JEM-2100 microscope operated at a 200 kV acceleration voltage. Atomic force microscopy (AFM) study of NSs on Si substrates was conducted in tapping mode using a Hitachi AFM5000II system. Thermogravimetric (TG) analysis was carried out using a Rigaku TG-DTA8122 instrument. Brunauer–Emmett–Teller (BET) specific surface areas were determined by  $\text{N}_2$  adsorption–desorption measurements using a Quantachrome Autosorb-1 analyzer. X-ray total scattering and pair distribution function (PDF) analyses were per-

formed on the BL04B2 beamline at the Super Photon Ring-8 GeV (SPring-8) facility in Hyogo, Japan. The incident beam energy was 112.9232 keV ( $\lambda = 0.109795 \text{ \AA}$ ).

## 3. Results and discussion

### 3.1. Binary CoNi hydroxide NCs

Binary CoNi hydroxide NCs were obtained by introducing Ni species into preformed Co hydroxide NCs, as schematically illustrated in Fig. 1a. As shown in Fig. S1a, pristine Co hydroxide NCs display uniform cone-shaped morphologies with distinct hollow interiors. Similar nanocone architectures were observed for  $\text{Co}_4\text{Ni}_1$ ,  $\text{Co}_3\text{Ni}_1$ , and  $\text{Co}_2\text{Ni}_1$  hydroxides (Fig. S1b–d), indicating that incorporating a moderate amount of Ni does not disrupt the conical framework. Nevertheless, further increasing the Ni proportion leads to a gradual deterioration of the nanocone structure. For the  $\text{Co}_1\text{Ni}_1$  sample (Fig. S1e), nanoplatelets emerge and partially decorate the surfaces of the NCs. In contrast, pure Ni hydroxide, as presented in Fig. S1f, predominantly exhibits a nanoplatelet-like morphology. These observations indicate that maintaining a Co-rich composition is essential for the formation and preservation of well-defined nanocone architectures. The EDS analysis summarized in Table S1 confirms that the actual Co:Ni atomic ratios in the CoNi hydroxides closely match the targeted compositions. As the designed Co:Ni ratio decreases from 4:1 to 1:1, the Co content correspondingly decreases while the Ni fraction increases. This composition evolution clearly indicates that the metal ions were successfully incorporated into the hydroxide framework, consistent with the designed stoichiometry.

Fig. S2 presents the XRD patterns of CoNi hydroxide NCs prepared with different Co/Ni ratios. All compositions display pronounced basal reflections corresponding to an interlayer spacing of 2.5 nm, which is characteristic of  $\text{DS}^-$ -intercalated  $\alpha$ -phase hydroxides and substantially larger than that of conventional brucite-type hydroxides (0.46 nm). These results indi-

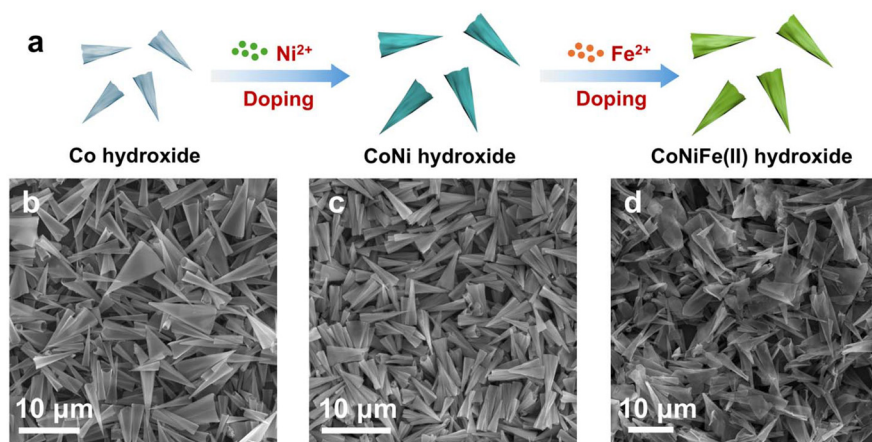


**Fig. 1** Synthesis of hydroxide NCs with different compositions. (a) Schematic illustration. SEM images of (b) Co hydroxide, (c)  $\text{Co}_3\text{Ni}_1$  hydroxide, and (d)  $\text{Co}_3\text{Ni}_1\text{Fe(II)}$  hydroxide.

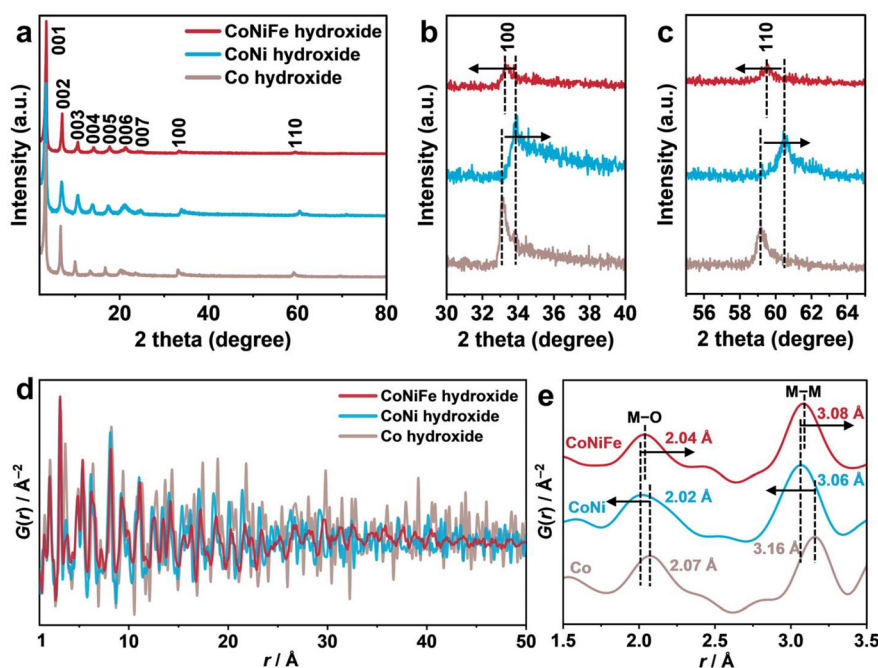


Fig. 2 (a–c) XRD patterns of  $\text{Co}_3\text{Ni}_1\text{Fe}_1$  hydroxide,  $\text{Co}_3\text{Ni}_1$  hydroxide, and Co hydroxide. PDF patterns of (d) high- $r$  and (e) low- $r$  regions.

cate that the layered framework is well preserved upon Ni incorporation. With increasing Ni content, both the 100 and 110 reflections gradually shift toward higher diffraction angles, reflecting a contraction of the in-plane lattice parameter  $a$ . This trend is consistent with partial substitution by  $\text{Ni}^{2+}$ , whose ionic radius (69 pm in  $\text{O}_h$  and 55 pm in  $\text{T}_d$ ) is smaller than that of  $\text{Co}^{2+}$  (74 pm in  $\text{O}_h$  and 58 pm in  $\text{T}_d$ ). In contrast, pure Ni hydroxide exhibits two distinct sets of diffraction peaks: one associated with a  $\text{DS}^-$ -intercalated  $\alpha$  phase and the other corresponding to a brucite-type structure without intercalation of any interlayer anions. The coexistence of the brucite phase likely originates from the limited ability of  $\text{Ni}^{2+}$  to adopt  $\text{T}_d$  coordination with  $\text{DS}^-$ , which is crucial for the formation of the  $\alpha$ -phase nanocone structure.

### 3.2. Ternary $\text{CoNiFe}(n)$ hydroxide NCs

SEM images in Fig. 1b–d reveal that the three hydroxide products retain well-defined nanocone architectures, demonstrating that compositional tuning does not fundamentally alter the overall morphology. Notably, the CoNiFe hydroxides exhibit a slight degradation in the conical structure compared with their Co and CoNi counterparts, implying that multimetal incorporation influences the crystal growth behavior and nanocone formation process. XRD patterns of the NCs with different compositions, represented by  $\text{Co}_3\text{Ni}_1\text{Fe}_1$  hydroxide,  $\text{Co}_3\text{Ni}_1$  hydroxide, and Co hydroxide, are shown in Fig. 2a. All the hydroxide NCs display a series of sharp 00 $l$  reflections, confirming the preservation of a well-defined layered structure. The low-angle basal reflections remain essentially unchanged across different compositions, indicating that the introduction of Ni and Fe does not significantly affect the basal lattice

framework. On the other hand, the enlarged views in Fig. 2b and c reveal a slight shift of the 100 and 110 peaks toward higher angles for CoNi hydroxide relative to Co hydroxide, indicating a contraction of in-plane lattice parameters induced by Ni incorporation. In contrast, the in-plane peaks of CoNiFe hydroxide shift to lower angles compared with those of CoNi hydroxide, reflecting the lattice expansion resulting from the larger ionic radius of  $\text{Fe}^{2+}$  (78 pm in  $\text{O}_h$  and 63 pm in  $\text{T}_d$ ) than those of  $\text{Co}^{2+}$  and  $\text{Ni}^{2+}$ . The variations in lattice spacing therefore confirm the successful incorporation of Ni and Fe into the host layers, accompanied by corresponding modifications of the local coordination environment within the hydroxide framework.

To probe the local atomic structure, PDF analysis was performed on hydroxides with different compositions. As shown in Fig. 2d, PDF profiles gradually decay with increasing  $r$ , which corresponds to longer-range atomic pair correlations in real space, reflecting the finite structural coherence length of the nanostructured hydroxides. Moreover, the intensities in the high- $r$  region progressively weaken from Co hydroxide to CoNi hydroxide and further to CoNiFe hydroxide, indicating a gradual reduction in long-range structural order upon multi-component incorporation.<sup>47</sup> This attenuation of PDF oscillations suggests an increased degree of structural disorder and a shortened coherence length induced by the successive introduction of Ni and Fe.<sup>48,49</sup> Such structural distortions are accompanied by modifications in the local coordination environment, which can alter the electronic structure of active sites and thereby influence the adsorption behavior of OER intermediates.<sup>25,35</sup> The low- $r$  region in Fig. 2e highlights distinct coordination features, where the peak at approximately



2.0 Å is assigned to M–O bonds, while the peak near 3.0 Å arises from M–M atomic correlations. Compared with Co hydroxide, both the M–O and M–M peaks of CoNi hydroxide shift to slightly shorter distances, indicating lattice contraction induced by Ni incorporation. In contrast, upon further introduction of Fe, the corresponding M–O and M–M peaks of CoNiFe hydroxide shift toward longer distances relative to those of CoNi hydroxide, reflecting lattice expansion. These systematic shifts in both M–O and M–M distances unequivocally confirm the successful incorporation of Ni and Fe into the host layers and the associated modification of the local coordination environment, which are consistent with the XRD observations.

### 3.3. Ternary CoNiFe(III) LDH NCs

A topochemical oxidation procedure shown in Fig. 3 was employed to transform the hydroxide NCs into an LDH phase. During this treatment,  $I_2$  served as an oxidizing agent to convert  $Fe^{2+}$  into  $Fe^{3+}$ , while  $I^-$  anions were simultaneously intercalated into the interlayer galleries to maintain charge balance. This process resulted in the formation of a CoNiFe(III) LDH with mixed  $T_d$  and  $O_h$  coordination (referred to as CoNiFe LDH $_{T_d/O_h}$ ). Fig. S3 displays the structural evolution of NCs prepared with a representative Co : Ni : Fe ratio of 3 : 1 : 1. XRD patterns along the  $c$ -axis exhibit negligible changes, which can be attributed to the smaller ionic radius of  $I^-$  relative to that of  $DS^-$ , leading to minimal variation in the interlayer spacing. In contrast, the in-plane 100 and 110 reflections of CoNiFe LDH $_{T_d/O_h}$  shift to higher angles compared to those of CoNiFe hydroxide, originating from lattice contraction induced by the oxidation of  $Fe^{2+}$  to  $Fe^{3+}$ , as  $Fe^{3+}$  possesses a significantly smaller ionic radius (65 pm in  $O_h$  and 49 pm in  $T_d$ ) than  $Fe^{2+}$  (78 pm in  $O_h$  and 63 pm in  $T_d$ ).

In addition, a series of CoNiFe LDH $_{T_d/O_h}$  samples with different Co, Ni, and Fe ratios were synthesized and characterized by SEM. As presented in Fig. S4, the samples with Co : Ni : Fe ratios of 8 : 1 : 1, 7 : 2 : 1, 7 : 2 : 2, and 7 : 1 : 2 all

retain well-defined and uniform nanocone structures. In contrast, increasing the Fe proportion to a ratio of 6 : 1 : 3 led to the collapse of the nanocone architecture, indicating that excessive Fe incorporation compromises structural stability. The corresponding elemental compositions determined by EDS are summarized in Table S2. Notably, the measured Fe contents are consistently lower than the nominal values, implying that Fe cannot be incorporated into the host layers in full stoichiometric proportions. This observation suggests that only a limited amount of Fe can be accommodated within the CoNi hydroxide lattice, likely due to disparities in ionic size or coordination tendencies. The XRD patterns in Fig. S5 further confirm that most of the CoNiFe LDH $_{T_d/O_h}$  samples retain the characteristic layered structure with an expanded interlayer spacing of approximately 2.5 nm, except for the Fe-rich sample with a Co : Ni : Fe ratio of 6 : 1 : 3. For the Fe-rich composition, the disappearance of the 001 and 002 peaks indicates the reduction in long-range order along the  $c$ -axis, which may result from poor crystallinity or incomplete interlayer anion intercalation.

Fig. 4a shows a SEM image of CoNiFe LDH $_{T_d/O_h}$ , where the nanocone morphology is well preserved after oxidation, indicating the topotactic transformation process. The TEM image in Fig. 4b further reveals that CoNiFe LDH $_{T_d/O_h}$  NCs possess a hollow interior, with an average length of approximately 6  $\mu m$  and a base diameter of around 1  $\mu m$ . The HRTEM image in Fig. 4c displays clearly resolved lattice fringes with an interlayer spacing of 2.5 nm, which is consistent with the value obtained from the XRD analysis. The SAED pattern in Fig. 4d can be indexed to the in-plane ([001] zone-axis) diffraction of the hexagonal structure with a lattice constant of  $a = 0.31$  nm. In addition, based on the TG profile in Fig. S6 together with the corresponding EDS analysis, the chemical composition of CoNiFe LDH $_{T_d/O_h}$  NCs with a designed Co : Ni : Fe ratio of 3 : 1 : 1 is estimated to be  $Co_{0.68}Ni_{0.23}Fe_{0.09}(OH)_{1.81}DS_{0.19}I_{0.09} \cdot 0.95H_2O$ .

XPS was employed to investigate the electronic structure changes induced by Fe incorporation into CoNi hydroxide. The

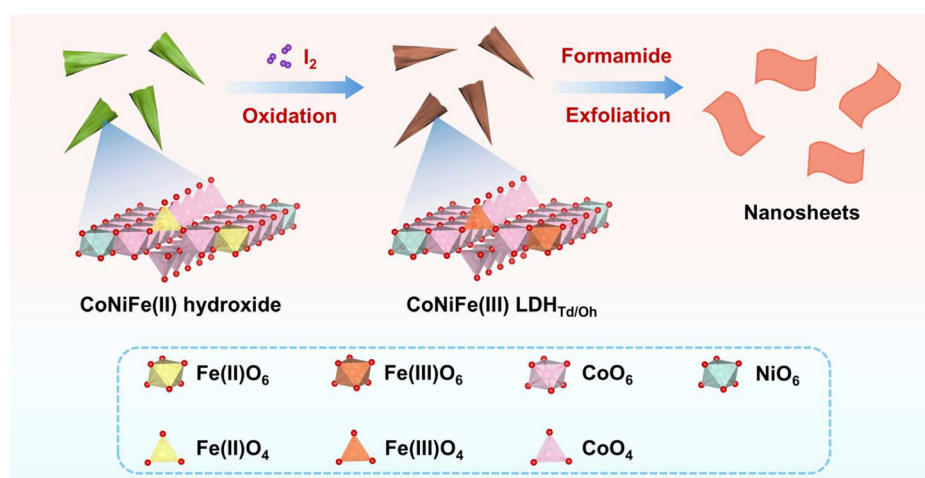


Fig. 3 Schematic illustration of topochemical oxidation and exfoliation processes.

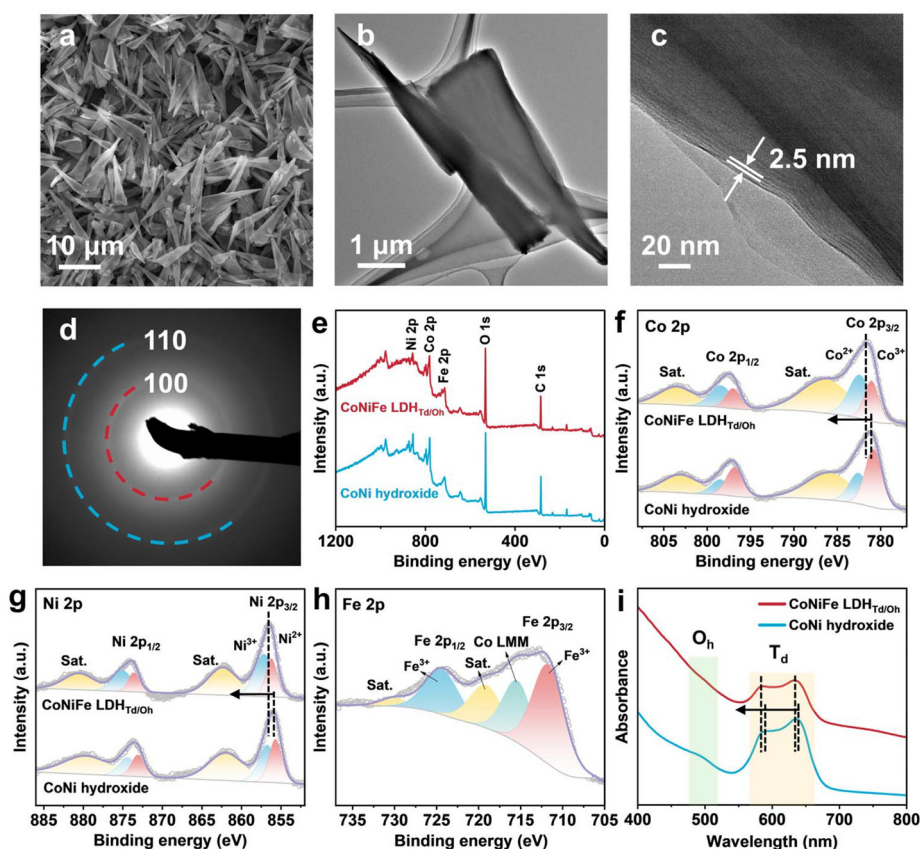


Fig. 4 (a) SEM image, (b) TEM image, (c) HRTEM image, and (d) SAED pattern. XPS spectra of (e) survey scan, (f) Co 2p, (g) Ni 2p, and (h) Fe 2p. (i) UV-vis spectra of CoNiFe LDH<sub>Td/Oh</sub> and CoNi hydroxide.

XPS survey spectra in Fig. 4e confirm the presence of Co, Ni, Fe, and O in CoNiFe LDH<sub>Td/Oh</sub>. The high-resolution Co 2p and Ni 2p spectra provide detailed insights into the oxidation states and local electronic environments of metal centers. As shown in Fig. 4f, the Co 2p peaks can be deconvoluted into contributions from Co<sup>2+</sup> and Co<sup>3+</sup>, accompanied by characteristic satellite features at higher binding energies. Similarly, the Ni 2p spectra in Fig. 4g contain well-defined Ni<sup>2+</sup> and Ni<sup>3+</sup> signals along with shake-up satellites. The Fe 2p spectrum, presented in Fig. 4h, displays a broad envelope comprising the Fe 2p<sub>3/2</sub> and Fe 2p<sub>1/2</sub> components, overlapped with the Co LMM Auger signal and characteristic shake-up satellites. Despite this convolution, the distinct Fe<sup>3+</sup> features remain clearly identifiable, confirming that Fe exists predominantly in the trivalent state after oxidation. These confirm the coexistence of mixed-valence Co and Ni species in CoNi hydroxide and CoNiFe LDH<sub>Td/Oh</sub>. Notably, upon Fe incorporation, both Co and Ni peaks shift toward lower binding energies. Although the shift direction is similar, the underlying electronic responses are distinct. This behavior can be attributed to charge redistribution within the LDH<sub>Td/Oh</sub> layers induced by Fe<sup>3+</sup> incorporation, which is governed by the distinct coordination environments of Co and Ni. Octahedrally coordinated Ni sites, with stronger metal–oxygen covalent bonding, tend toward electron depletion, while Co sites with mixed tetra-

hedral/octahedral coordination support electron accumulation. To maintain overall charge neutrality, a site-selective internal electron rearrangement occurs through the M–O–M network, resulting in partial oxidation of Ni and reduction of Co. This manifests as a coordination-dependent, cooperative electronic modulation within the multimetal framework. The clear identification of Co<sup>2+</sup>/Co<sup>3+</sup> and Ni<sup>2+</sup>/Ni<sup>3+</sup> signatures further confirms the successful integration of Fe into the host lattice and its pronounced influence on the local electronic environment. On the other hand, diffuse UV-vis absorption spectra were used to explore the coordination symmetry of CoNiFe LDH<sub>Td/Oh</sub>. As shown in Fig. 4i, a broad absorption band at around 500 nm is associated with Co species in O<sub>h</sub> coordination environments, whereas two pronounced bands near ~585 nm and ~635 nm originate from the characteristic d–d electronic transitions of Co in T<sub>d</sub> sites.<sup>26,50</sup> Compared with CoNi hydroxide, the O<sub>h</sub>-related absorption band of CoNiFe LDH<sub>Td/Oh</sub> becomes weaker, accompanied by a slight blue shift of T<sub>d</sub> peaks, suggesting the coexistence of O<sub>h</sub> and T<sub>d</sub> coordination for Fe species.<sup>32</sup>

### 3.4. Exfoliation of LDH NCs

CoNiFe LDH<sub>Td/Oh</sub> NCs with interlayer DS<sup>−</sup> anions can be readily delaminated into ultrathin NSs in formamide under ultrasonication. As shown in Fig. 5, AFM images of Co<sub>8</sub>Ni<sub>1</sub>Fe<sub>1</sub>,

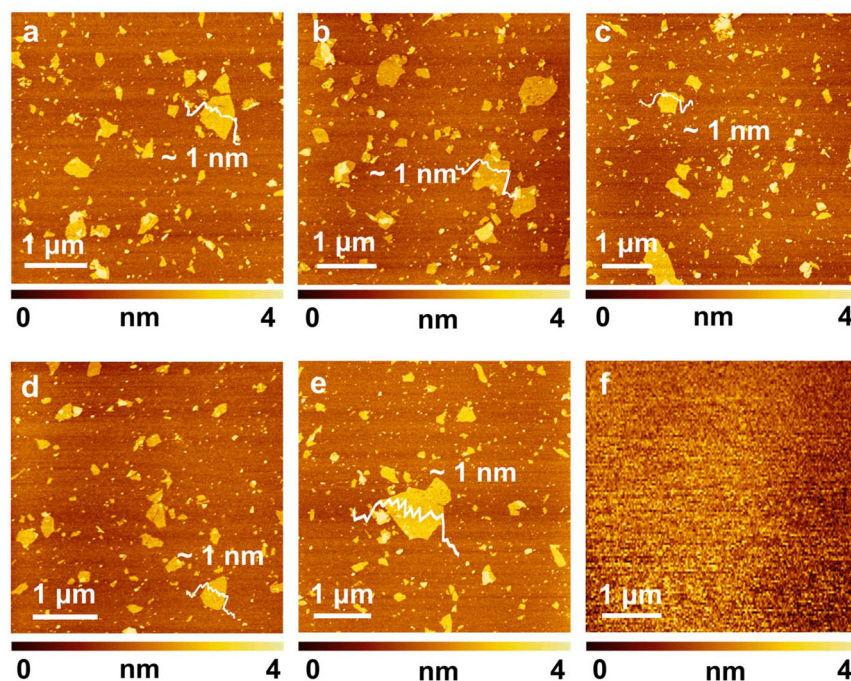


**Fig. 5** AFM images of CoNiFe LDH<sub>Td/O<sub>h</sub></sub> NSs with different metal ratios: (a) Co<sub>8</sub>Ni<sub>1</sub>Fe<sub>1</sub>, (b) Co<sub>7</sub>Ni<sub>2</sub>Fe<sub>1</sub>, (c) Co<sub>7</sub>Ni<sub>2</sub>Fe<sub>2</sub>, (d) Co<sub>3</sub>Ni<sub>1</sub>Fe<sub>1</sub>, (e) Co<sub>7</sub>Ni<sub>1</sub>Fe<sub>2</sub>, and (f) Co<sub>6</sub>Ni<sub>1</sub>Fe<sub>3</sub>. The values represent the cross-sectional profile of the nanosheet.

Co<sub>7</sub>Ni<sub>2</sub>Fe<sub>1</sub>, Co<sub>7</sub>Ni<sub>2</sub>Fe<sub>2</sub>, Co<sub>3</sub>Ni<sub>1</sub>Fe<sub>1</sub>, and Co<sub>7</sub>Ni<sub>1</sub>Fe<sub>2</sub> samples display well-dispersed, sheet-like objects with thicknesses around 1 nm and lateral dimensions from tens to several hundred nanometers. These features are consistent with previous reports on monolayer LDH NSs.<sup>26</sup> The measured thickness slightly exceeds the crystallographic thickness (~0.48 nm), likely due to the peculiar T<sub>d</sub>/O<sub>h</sub> coordination or adsorption of formamide and water molecules on the nanosheet surfaces.<sup>51,52</sup> In contrast, due to an insufficient DS<sup>−</sup> intercalation, the Co<sub>6</sub>Ni<sub>1</sub>Fe<sub>3</sub> sample could not be well exfoliated, and no NSs are observed in Fig. 5f.

Synchrotron in-plane diffractions of Co hydroxide, CoNi hydroxide, and CoNiFe LDH<sub>Td/O<sub>h</sub></sub> NSs are compared in Fig. 6a. The patterns can be indexed to the 10, 11, and 20 reflections,

which are characteristic of the 2D hexagonal symmetry of hydroxide NSs. These well-defined in-plane reflections confirm the high crystallinity and well-preserved 2D lattice across all compositions. Compared with Co hydroxide, CoNi hydroxide shows a shift toward in-plane lattice contraction. In addition, the reflections of CoNiFe LDH<sub>Td/O<sub>h</sub></sub> display a further slight contraction relative to those of its CoNi counterpart, which can be attributed to the successful oxidation of Fe<sup>2+</sup> to Fe<sup>3+</sup>. Such systematic peak shifts are fully consistent with the powder XRD results, further substantiating the effective incorporation of Fe<sup>3+</sup> and its influence on the local coordination environment within the LDH<sub>Td/O<sub>h</sub></sub> structure. In addition to the peak shifts, the gradual attenuation of the diffraction intensity is observed from Co hydroxide to CoNi hydroxide and CoNiFe LDH, imply-

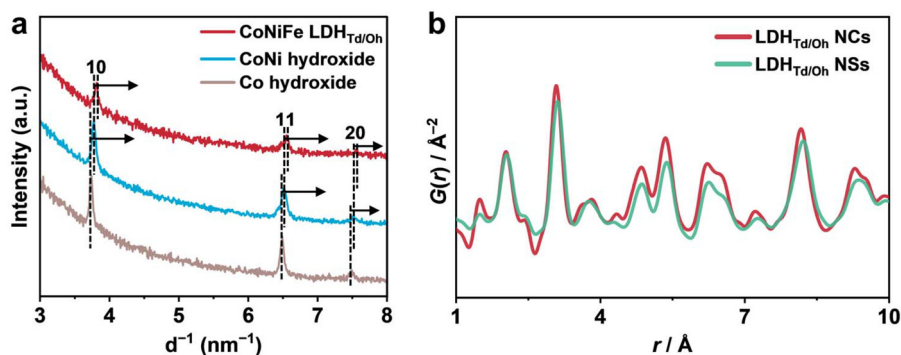


**Fig. 6** (a) Synchrotron in-plane XRD patterns of Co hydroxide, CoNi hydroxide, and CoNiFe LDH<sub>Td/O<sub>h</sub></sub> NSs. (b) PDF patterns of CoNiFe LDH<sub>Td/O<sub>h</sub></sub> NCs and NSs.



ing a reduction in in-plane crystallographic coherence. This behavior is likely associated with lattice distortion and increased structural disorder induced by heteroatom doping. To further elucidate the structural differences between CoNiFe LDH<sub>Td/Oh</sub> NCs and their exfoliated nanosheet counterparts, PDF analysis was performed. As shown in Fig. 6b and Fig. S7, both samples display almost identical peak positions throughout the entire  $r$  range, indicating that the primary local coordination environment around the metal sites is largely preserved after exfoliation. In contrast, the exfoliated NSs exhibit significantly attenuated peak intensities, reflecting enhanced local disorders typically associated with reduced dimensionality.<sup>49</sup> The attenuated peak intensities further suggest a reduced average coordination number, which can be attributed to both the loss of interlayer stacking and the decreased lateral size upon exfoliation. Specifically, the disruption of interlayer correlations reduces atomic pair contributions along the out-of-plane direction, while the reduced nanosheet size increases the fraction of under-coordinated surface and edge sites, leading to the weakened PDF signals.

### 3.5. Electrochemical performance

The OER performance of CoNi hydroxide NCs with different Co/Ni ratios was first examined. As shown in the LSV curves in Fig. S8a, the introduction of an appropriate amount of Ni markedly enhances the catalytic activity compared with that with pristine monometal (Co and Ni) hydroxides. The overpotentials at 10 mA cm<sup>-2</sup> summarized in Fig. S8b further confirm this trend. Among the catalysts, Co<sub>3</sub>Ni<sub>1</sub> hydroxide achieves the lowest overpotential of 339 mV, outperforming Co(OH)<sub>2</sub> (377 mV) and Ni(OH)<sub>2</sub> (413 mV). These results indicate that an optimized Co–Ni composition is essential for achieving high activity, while excessive Ni incorporation leads to reduced performance. EIS measurements in Fig. S8c provide additional insight into the charge-transfer behavior. Co<sub>3</sub>Ni<sub>1</sub> hydroxide shows the smallest Nyquist semicircle, corresponding to the lowest charge-transfer resistance ( $R_{ct}$ ). This observation demonstrates that moderate Ni incorporation not only improves the intrinsic catalytic characteristics but also facilitates more effective interfacial charge transport. In contrast, Ni-rich samples and pure Ni(OH)<sub>2</sub> present much larger semicircles, indicating sluggish reaction kinetics and less favorable electron-transfer behavior.

The OER activities of CoNiFe LDH<sub>Td/Oh</sub> NCs with various elemental compositions were further systematically evaluated. As shown in the LSV curves in Fig. S9a, the Co<sub>3</sub>Ni<sub>1</sub>Fe<sub>1</sub> LDH<sub>Td/Oh</sub> sample delivers markedly higher current densities at lower overpotentials, indicating its superior catalytic performance. In contrast, compositions enriched in Co or Fe (e.g., Co<sub>8</sub>Ni<sub>1</sub>Fe<sub>1</sub> and Co<sub>6</sub>Ni<sub>1</sub>Fe<sub>3</sub>) exhibit noticeably inferior activity. As summarized in Fig. S9b, Co<sub>3</sub>Ni<sub>1</sub>Fe<sub>1</sub> LDH<sub>Td/Oh</sub> NCs achieve the lowest overpotential of 280 mV at 10 mA cm<sup>-2</sup>, outperforming not only the other ternary formulations but also their binary counterparts, demonstrating the beneficial role of appropriate Fe incorporation in boosting OER activity. The catalytic kinetics were further assessed from the Tafel slopes in Fig. S9c.

Co<sub>3</sub>Ni<sub>1</sub>Fe<sub>1</sub> LDH<sub>Td/Oh</sub> NCs exhibit the smallest slope (53.3 mV dec<sup>-1</sup>), which indicates more favorable reaction kinetics. This reduction in the Tafel slope correlates well with the lower overpotential, confirming that moderate Fe doping effectively accelerates the OER process. Moreover, the Nyquist plots in Fig. S9d show that Co<sub>3</sub>Ni<sub>1</sub>Fe<sub>1</sub> LDH<sub>Td/Oh</sub> NCs yield the smallest semicircle radius, corresponding to the lowest  $R_{ct}$  among the tested samples. This observation further underscores the kinetic advantages arising from the optimized Co–Ni–Fe composition.

The LSV curves in Fig. 7a clearly demonstrate that the ternary CoNiFe LDH<sub>Td/Oh</sub> NCs deliver the highest catalytic activity, achieving markedly higher current densities at lower applied potentials. Both the binary CoNi hydroxide NCs and the pristine Co hydroxide NCs exhibit inferior activity, while RuO<sub>2</sub> shows only moderate performance under identical conditions. These trends are quantified by the overpotentials required to reach 10 mA cm<sup>-2</sup> and plotted in Fig. 7b. CoNiFe LDH<sub>Td/Oh</sub> NCs exhibit an overpotential of 280 mV, substantially lower than those of CoNi hydroxide NCs (339 mV) and Co hydroxide NCs (377 mV). This comparison indicates that Ni incorporation significantly enhances the intrinsic OER activity relative to its Co counterpart, while Fe doping leads to an additional and pronounced improvement in performance. The Tafel plots in Fig. 7c further confirm these findings. CoNiFe LDH<sub>Td/Oh</sub> NCs show the smallest Tafel slope (53.3 mV dec<sup>-1</sup>), indicating the accelerated reaction kinetics of the ternary composition. In contrast, CoNi hydroxide NCs and Co hydroxide NCs display notably larger Tafel slopes, reflecting slower kinetic processes. The improved kinetics of CoNiFe LDH<sub>Td/Oh</sub> NCs can be attributed to synergistic multimetal interactions and the edge-rich surface of the nanocone morphology, which may facilitate the formation and deprotonation of OER intermediates. Consistent with the kinetic analysis, the Nyquist plots in Fig. 7d reveal that CoNiFe LDH<sub>Td/Oh</sub> NCs possess the smallest semicircle radius, corresponding to the lowest  $R_{ct}$ . This further supports that introducing Fe enhances electron transport and interface reaction rates. In comparison, Co and CoNi hydroxide NCs show larger  $R_{ct}$  values. To gain insight into the ECSA, the  $C_{dl}$  was estimated from CV measurements conducted at various scan rates within the non-faradaic region (Fig. S10). As depicted in Fig. 7e, CoNiFe LDH<sub>Td/Oh</sub> NCs show the largest  $C_{dl}$  (79.4 mF cm<sup>-2</sup>), markedly exceeding those of CoNi hydroxide (43.0 mF cm<sup>-2</sup>) and Co hydroxide (18.4 mF cm<sup>-2</sup>). The results demonstrate that composition optimization plays decisive roles in increasing the density of accessible active sites. To evaluate the long-term durability, the CoNiFe LDH<sub>Td/Oh</sub> NC catalyst was examined by chronopotentiometry testing at a constant current density of 10 mA cm<sup>-2</sup> and the results are shown in Fig. 7f. The negligible potential fluctuation over 40 h demonstrates excellent operational stability under continuous OER conditions. In addition, the OER performance of CoNiFe LDH<sub>Td/Oh</sub> was compared with recently reported non-precious metal electrocatalysts, as summarized in Table S3. The results demonstrate that CoNiFe LDH<sub>Td/Oh</sub> exhibits OER activity surpassing that of many recently reported catalysts.



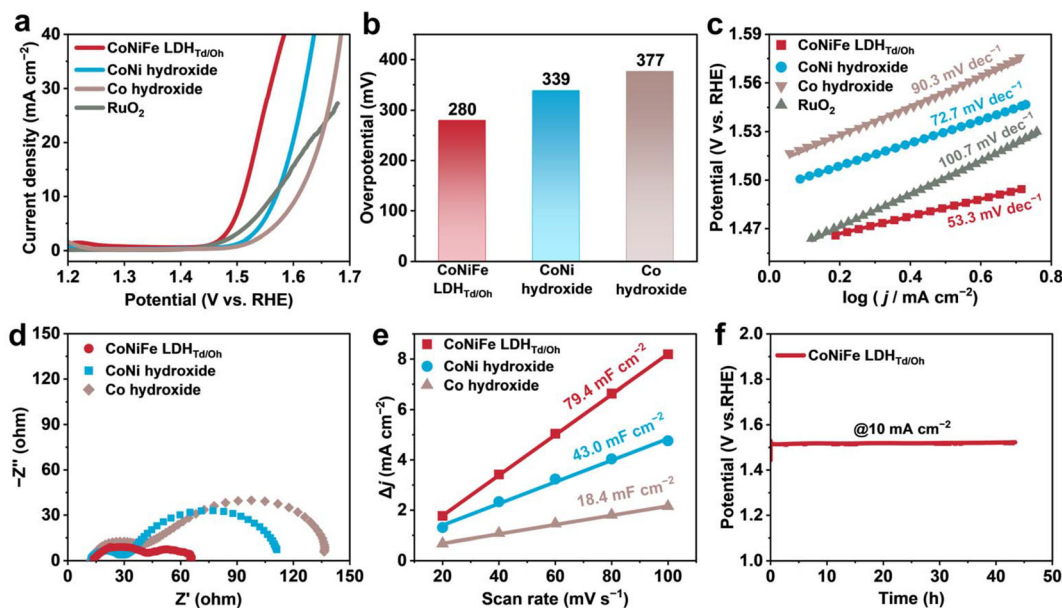


Fig. 7 Comparison of OER performance. (a) LSV curves, (b) overpotentials at  $10 \text{ mA cm}^{-2}$ , (c) Tafel slopes, (d) Nyquist plots, (e) current density differences versus scan rates measured in the non-faradaic ranges of CoNiFe LDH<sub>Td/O<sub>h</sub></sub> NCs, CoNi hydroxide NCs, Co hydroxide NCs, and commercial RuO<sub>2</sub>. (f) Chronopotentiometry test of CoNiFe LDH<sub>Td/O<sub>h</sub></sub> NCs.

In contrast, Co<sub>3</sub>Ni<sub>1</sub>Fe<sub>1</sub> LDH nanoplatelets with conventional O<sub>h</sub> coordination were also prepared *via* the same topochemical oxidation of CoNiFe brucite-type hydroxides using iodine. As shown in Fig. S11, due to the relatively lower Fe<sup>3+</sup> content, the resulting LDH nanoplatelets exhibit mixed-layer features with partial DS<sup>-</sup> intercalation and the occurrence of the second staging phase.<sup>31,53,54</sup> As revealed by the N<sub>2</sub> adsorption-desorption isotherms in Fig. S12, the LDH<sub>Td/O<sub>h</sub></sub> NCs possess a notably larger specific surface area ( $19.1 \text{ m}^2 \text{ g}^{-1}$ ) than the nanoplatelets ( $9.9 \text{ m}^2 \text{ g}^{-1}$ ), indicating a higher electrochemically accessible surface and a greater density of exposed active sites. Consistent with this structural advantage, the NCs exhibit a lower overpotential, faster reaction kinetics, and improved charge-transfer behavior compared with the nanoplatelets, as evidenced by the LSV, Tafel, and impedance analyses in Fig. S13. In addition, the larger ECSA of the NCs suggests more accessible active sites. The superior performance of LDH<sub>Td/O<sub>h</sub></sub> NCs can be attributed to the synergistic effects of the hollow nanocone morphology and the coexistence of Td/O<sub>h</sub> coordination environments, which together facilitate mass transport, enhance electronic conductivity, and optimize the intrinsic activity of the catalytic sites relative to conventional O<sub>h</sub> coordinated nanoplatelets.

The OER electrocatalytic activity of the exfoliated CoNiFe LDH<sub>Td/O<sub>h</sub></sub> NSs was also evaluated and compared with that of their nanocone counterparts under alkaline conditions. To facilitate the practical handling and utilization of the CoNiFe LDH<sub>Td/O<sub>h</sub></sub> NSs, they were flocculated using carbonate (CO<sub>3</sub><sup>2-</sup>) anions. The SEM image in Fig. 8a reveals that the flocculated product exhibits a loose, fluffy-like morphology composed of interconnected NSs. Such a porous architecture is expected to

enhance the accessible specific surface area, thereby facilitating subsequent processing and application. As shown in the XRD pattern of the flocculated product in Fig. 8b, a series of intense 00 $l$  reflections previously observed for the NCs disappear, indicating the disruption of long-range stacking order along the  $c$ -axis after exfoliation. Meanwhile, the  $d$ -spacing of the restacked NSs is determined to be  $0.79 \text{ nm}$ , which is consistent with CO<sub>3</sub><sup>2-</sup> intercalation within the interlayer galleries. Notably, the N<sub>2</sub> adsorption-desorption isotherms in Fig. 8c demonstrate that CoNiFe LDH<sub>Td/O<sub>h</sub></sub> NSs display a significantly higher adsorption capacity, corresponding to a much larger specific surface area of  $71.8 \text{ m}^2 \text{ g}^{-1}$  compared with  $19.1 \text{ m}^2 \text{ g}^{-1}$  for the NCs. This increase originates from the reduced lateral and stacking dimensions after exfoliation, leading to less ordered aggregation and more exposed surfaces. As a result, the flocculated nanosheet architecture forms a more open porous network, facilitating mass transport and thereby providing a structural basis for enhanced electrocatalytic performance. However, it should be noted that the restacked NSs exhibit relatively small interlayer spacing ( $\sim 0.79 \text{ nm}$ ), which may make the interlayer less accessible to the electrolyte. In contrast, the NCs possess a larger interlayer spacing ( $\sim 2.5 \text{ nm}$ ), which facilitates ion transport and improves the utilization of internal surfaces. As evidenced by the LSV curves in Fig. 8d, LDH<sub>Td/O<sub>h</sub></sub> NSs exhibit a significantly reduced overpotential of  $267 \text{ mV}$  at a current density of  $10 \text{ mA cm}^{-2}$ , which is markedly lower than that of the NCs, indicating substantially enhanced OER performance. According to the results in Fig. 8e, CoNiFe LDH<sub>Td/O<sub>h</sub></sub> NSs deliver a larger  $C_{dl}$  value ( $96.8 \text{ mF cm}^{-2}$ ) than CoNiFe LDH<sub>Td/O<sub>h</sub></sub> NCs ( $79.4 \text{ mF cm}^{-2}$ ), implying a higher ECSA. The smaller increase in  $C_{dl}$  relative to

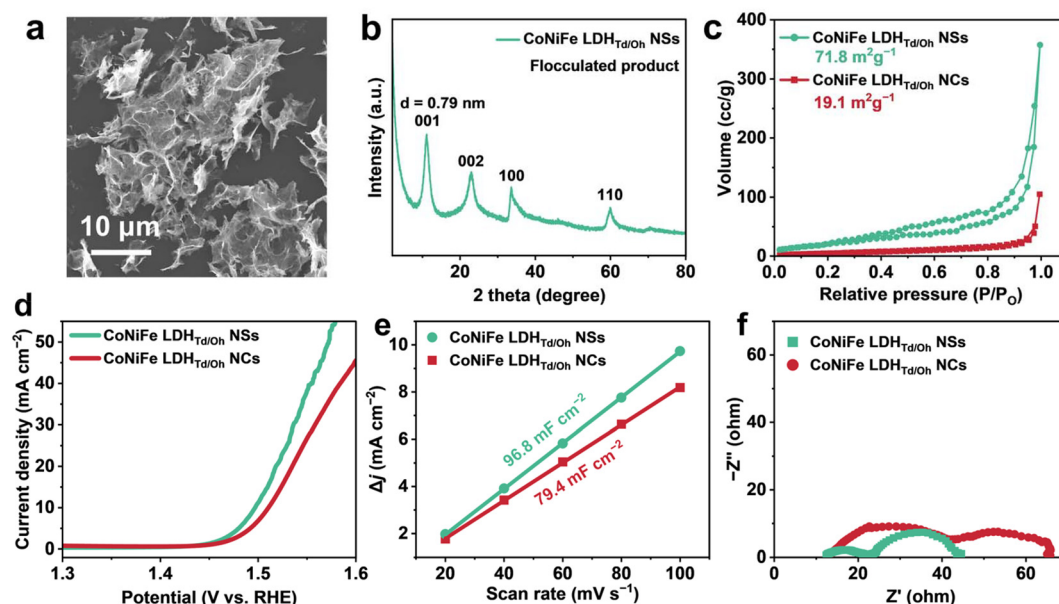


Fig. 8 (a) SEM image and (b) XRD pattern of flocculated NSs. (c)  $N_2$  adsorption–desorption isotherms. (d) LSV curves, (e) current density differences versus scan rates measured in the non-faradaic range, and (f) Nyquist plots.

the BET surface area reflects a trade-off between enhanced surface area and reduced electrochemical accessibility associated with the decreased interlayer spacing. Despite this limitation, the ultrathin NS structure still exposes more active sites to the electrolyte, resulting in an overall increase in ECSA and the observed performance enhancement. To decouple the contributions from active site density and intrinsic activity, the current densities were normalized by ECSA, as shown in Fig. S14. After normalization, CoNiFe LDH<sub>Td/Oh</sub> NSs exhibit slightly higher current density than NCs, suggesting that the performance enhancement is dominated by increased active site density, accompanied by a modest improvement in intrinsic activity due to structural and electronic modulation upon exfoliation. EIS was employed to investigate the charge-transfer properties of the catalysts. As illustrated in the Nyquist plots in Fig. 8f, the NSs display a smaller semicircle diameter than the NCs, corresponding to a reduced  $R_{ct}$ . The accelerated interfacial electron transport facilitates the adsorption and conversion of OER intermediates, thereby further promoting the reaction kinetics. Overall, the superior OER performance of the LDH<sub>Td/Oh</sub> NSs can be ascribed to the synergistic effects of enlarged ECSA and enhanced charge-transfer kinetics induced by the exfoliated nanosheet architecture.

## 4. Conclusions

Binary CoNi and ternary CoNiFe hydroxide NCs with mixed T<sub>d</sub>/O<sub>h</sub> coordination were successfully constructed *via* controlled Ni and Fe incorporation into Co-based hydroxide NCs, demonstrating an effective strategy for enhancing electrocatalytic activity through multimetal synergy. Systematic compositional

tuning of CoNi hydroxide NCs revealed that moderate Ni incorporation optimizes OER performance, with the Co<sub>3</sub>Ni<sub>1</sub> sample delivering a small overpotential of 339 mV at 10 mA cm<sup>-2</sup>. Subsequent Fe incorporation followed by a topochemical oxidative intercalation process yielded ternary CoNiFe LDH<sub>Td/Oh</sub>. Among the ternary systems, the NCs with a Co<sub>3</sub>Ni<sub>1</sub>Fe<sub>1</sub> composition exhibited the most favorable electrocatalytic performance, achieving the lowest overpotential of 280 mV at 10 mA cm<sup>-2</sup>, highlighting the critical role of Fe doping. Furthermore, the ternary LDH<sub>Td/Oh</sub> NCs were readily exfoliated into monolayer NSs with atomic-scale thickness. Owing to the enlarged specific surface area and increased exposure of active sites, the NSs displayed further enhanced OER performance relative to the NCs, with the overpotential further reduced to 267 mV. Overall, this work underscores the synergistic effects of compositional modulation, coordination engineering, and morphological design in advancing high-performance layered hydroxide electrocatalysts.

## Author contributions

Z. Zhang: conceptualization, investigation, methodology, data curation, formal analysis, and writing – original draft. X. Jiang: data analysis, validation, and writing – review & editing. N. Ma: investigation, formal analysis, and writing – review & editing. J. Zhang: formal analysis and writing – review & editing. E. Picheau: investigation and writing – review & editing. N. Sakai: investigation and writing – review & editing. T. Sasaki: supervision and writing – review & editing. R. Ma: conceptualization, funding acquisition, supervision, and writing – review & editing.

## Conflicts of interest

There are no conflicts to declare.

## Data availability

The data supporting this article have been included as part of the supplementary information (SI). Supplementary information: SEM, XRD, TG, PDF, and electrochemical measurements, and BET data. See DOI: <https://doi.org/10.1039/d6nr00271d>.

## Acknowledgements

This work was supported in part by the World Premier International Research Center Initiative (WPI), Ministry of Education, Culture, Sports, Science and Technology (MEXT), Japan. R. M. acknowledges support from JSPS KAKENHI (22H01916, 22K18956, 25K22208 and 26H02227). J. Z. acknowledges JSPS International Research Fellows (24KF0273). The in-plane XRD measurements were performed under the approval of the Photon Factory Program Advisory Committee (Proposal No. 2024G501). The XPS facility at NIMS Materials Analysis Station is gratefully acknowledged. We acknowledge BL04B2 beamlines at SPring-8 for the synchrotron X-ray total scattering experiments with the approval of JASRI (Proposal No. 2025A1067 and 2025B1248). A part of this work was supported by the Electron Microscopy Unit, National Institute for Materials Science (NIMS).

## References

- 1 Z. W. Seh, J. Kibsgaard, C. F. Dickens, I. Chorkendorff, J. K. Nørskov and T. F. Jaramillo, *Science*, 2017, **355**, eaad4998.
- 2 J. Lai, B. Huang, Y. Chao, X. Chen and S. Guo, *Adv. Mater.*, 2019, **31**, 1805541.
- 3 Y. Jiao, Y. Zheng, M. Jaroniec and S. Z. Qiao, *Chem. Soc. Rev.*, 2015, **44**, 2060–2086.
- 4 J. Song, C. Wei, Z.-F. Huang, C. Liu, L. Zeng, X. Wang and Z. J. Xu, *Chem. Soc. Rev.*, 2020, **49**, 2196–2214.
- 5 B. You, M. T. Tang, C. Tsai, F. Abild-Pedersen, X. Zheng and H. Li, *Adv. Mater.*, 2019, **31**, 1807001.
- 6 J. Zhang, Z. Zhang, R. Ma and T. Sasaki, *ACS Energy Lett.*, 2026, **11**, 101–110.
- 7 H. Sun, X. Xu, Z. Hu, L. H. Tjeng, J. Zhao, Q. Zhang, H.-J. Lin, C.-T. Chen, T.-S. Chan, W. Zhou and Z. Shao, *J. Mater. Chem. A*, 2019, **7**, 9924–9932.
- 8 M. Tahir, L. Pan, F. Idrees, X. Zhang, L. Wang, J.-J. Zou and Z. L. Wang, *Nano Energy*, 2017, **37**, 136–157.
- 9 J. Yang, J. K. Cooper, F. M. Toma, K. A. Walczak, M. Favaro, J. W. Beeman, L. H. Hess, C. Wang, C. Zhu, S. Gul, J. Yano, C. Kisielowski, A. Schwartzberg and I. D. Sharp, *Nat. Mater.*, 2017, **16**, 335–341.
- 10 K. A. Stoerzinger, L. Qiao, M. D. Biegalski and Y. Shao-Horn, *J. Phys. Chem. Lett.*, 2014, **5**, 1636–1641.
- 11 T. Audichon, T. W. Napporn, C. Canaff, C. Morais, C. Comminges and K. B. Kokoh, *J. Phys. Chem. C*, 2016, **120**, 2562–2573.
- 12 H. Over, *ACS Catal.*, 2021, **11**, 8848–8871.
- 13 M. Gong and H. Dai, *Nano Res.*, 2015, **8**, 23–39.
- 14 M. S. Burke, L. J. Enman, A. S. Batchellor, S. Zou and S. W. Boettcher, *Chem. Mater.*, 2015, **27**, 7549–7558.
- 15 K. Zhang and R. Zou, *Small*, 2021, **17**, 2100129.
- 16 H. Sun, Z. Yan, F. Liu, W. Xu, F. Cheng and J. Chen, *Adv. Mater.*, 2020, **32**, 1806326.
- 17 Z. Li, D. Liao, G. Tian, X. Fan, X. Chai, W. Chang, Y. Gao, B. Yuan, Z. Li, F. Wei and C. Zhang, *J. Am. Chem. Soc.*, 2025, **147**, 32548–32559.
- 18 M. Xu and M. Wei, *Adv. Funct. Mater.*, 2018, **28**, 1802943.
- 19 Y. Wang, M. Zhang, Y. Liu, Z. Zheng, B. Liu, M. Chen, G. Guan and K. Yan, *Adv. Sci.*, 2023, **10**, 2207519.
- 20 G. Chen, H. Wan, W. Ma, N. Zhang, Y. Cao, X. Liu, J. Wang and R. Ma, *Adv. Energy Mater.*, 2020, **10**, 1902535.
- 21 L. Tian, K. Wang, H. Wo, Z. Li, M. Song, J. Li, T. Li and X. Du, *J. Taiwan Inst. Chem. Eng.*, 2019, **96**, 273–280.
- 22 Z. Li, D. Liu, X. Lu, M. Du, Z. Chen, J. Teng, R. Sha and L. Tian, *Dalton Trans.*, 2022, **51**, 1527–1532.
- 23 S. Tang, Y. Zhou, X. Lu, Z. Chen, Z. Huang, Z. Li and L. Tian, *J. Alloys Compd.*, 2022, **924**, 166415.
- 24 X. Feng, Q. Jiao, W. Chen, Y. Dang, Z. Dai, S. L. Suib, J. Zhang, Y. Zhao, H. Li and C. Feng, *Appl. Catal., B*, 2021, **286**, 119869.
- 25 Z. Zhang, R. Zhang, N. Ma, E. Picheau, L. K. Shrestha, W. Zhou, X. Liu, Y. Sugahara, T. Sasaki and R. Ma, *Small*, 2025, **21**, 2502344.
- 26 X. Liu, R. Ma, Y. Bando and T. Sasaki, *Angew. Chem., Int. Ed.*, 2010, **49**, 8253–8256.
- 27 X. Liu, R. Ma, Y. Bando and T. Sasaki, *Adv. Mater.*, 2012, **24**, 2148–2153.
- 28 X. Liu, R. Ma, Y. Bando and T. Sasaki, *Adv. Funct. Mater.*, 2014, **24**, 4292–4302.
- 29 L. Jia, H. Wan, X. Liu, G. Chen, N. Zhang, J. Li, W. Zhou, Y. Cao, R. Ma and G. Qiu, *ChemSusChem*, 2019, **12**, 5274–5281.
- 30 R. Ma, Z. Liu, K. Takada, N. Iyi, Y. Bando and T. Sasaki, *J. Am. Chem. Soc.*, 2007, **129**, 5257–5263.
- 31 R. Ma, J. Liang, K. Takada and T. Sasaki, *J. Am. Chem. Soc.*, 2011, **133**, 613–620.
- 32 Y. He, X. Liu, G. Chen, J. Pan, A. Yan, A. Li, X. Lu, D. Tang, N. Zhang, T. Qiu, R. Ma and T. Sasaki, *Chem. Mater.*, 2020, **32**, 4232–4240.
- 33 A. Karmakar, K. Karthick, S. S. Sankar, S. Kumaravel, R. Madhu and S. Kundu, *J. Mater. Chem. A*, 2021, **9**, 1314–1352.
- 34 J. Wang and H. C. Zeng, *ACS Appl. Energy Mater.*, 2018, **1**, 4998–5007.
- 35 Z. Zhang, Z. Zheng, N. Ma, E. Picheau, N. Sakai, Y. Sugahara, T. Sasaki and R. Ma, *Chem. Eng. J.*, 2025, **509**, 161248.

- 36 Y. Lin, H. Wang, C.-K. Peng, L. Bu, C.-L. Chiang, K. Tian, Y. Zhao, J. Zhao, Y.-G. Lin, J.-M. Lee and L. Gao, *Small*, 2020, **16**, 2002426.
- 37 J. Saha and F. A. Molla, *Nanoscale*, 2025, **17**, 26050–26056.
- 38 M.-Y. Xie, J.-R. Huang, H. Wan, J. Nie, M.-H. Xian, Z.-Y. Ou-Yang, G.-F. Huang and W.-Q. Huang, *Appl. Phys. Lett.*, 2025, **126**, 153901.
- 39 J. Nie, J. Shi, L. Li, M.-Y. Xie, Z.-Y. Ouyang, M.-H. Xian, G.-F. Huang, H. Wan, W. Hu and W.-Q. Huang, *Adv. Funct. Mater.*, 2025, **35**, 2414493.
- 40 J.-R. Huang, M.-Y. Xie, M.-H. Xian, Y. Luo, J.-H. Nie, Z.-Y. Ou-Yang, Q.-X. Wang, G.-F. Huang and W.-Q. Huang, *Appl. Phys. Lett.*, 2025, **127**, 103905.
- 41 S. Anantharaj, S. Kundu and S. Noda, *Nano Energy*, 2021, **80**, 105514.
- 42 J. Wei, J. Zhu, R. Jin, Y. Liu, G. Liu, M.-H. Fan, M. Liu, D. Jiang and J. Zeng, *J. Am. Chem. Soc.*, 2025, **147**, 13502–13511.
- 43 L. Trotochaud, S. L. Young, J. K. Ranney and S. W. Boettcher, *J. Am. Chem. Soc.*, 2014, **136**, 6744–6753.
- 44 R. Ma, J. Liang, X. Liu and T. Sasaki, *J. Am. Chem. Soc.*, 2012, **134**, 19915–19921.
- 45 S. Niu, W.-J. Jiang, T. Tang, L.-P. Yuan, H. Luo and J.-S. Hu, *Adv. Funct. Mater.*, 2019, **29**, 1902180.
- 46 C. C. L. McCrory, S. Jung, J. C. Peters and T. F. Jaramillo, *J. Am. Chem. Soc.*, 2013, **135**, 16977–16987.
- 47 M. W. Terban and S. J. L. Billinge, *Chem. Rev.*, 2022, **122**, 1208–1272.
- 48 S. J. L. Billinge and M. G. Kanatzidis, *Chem. Commun.*, 2004, 749–760.
- 49 D. A. Keen and A. L. Goodwin, *Nature*, 2015, **521**, 303–309.
- 50 R. Ma, Z. Liu, K. Takada, K. Fukuda, Y. Ebina, Y. Bando and T. Sasaki, *Inorg. Chem.*, 2006, **45**, 3964–3969.
- 51 W. Ma, R. Ma, C. Wang, J. Liang, X. Liu, K. Zhou and T. Sasaki, *ACS Nano*, 2015, **9**, 1977–1984.
- 52 R. Ma and T. Sasaki, *Adv. Mater.*, 2010, **22**, 5082–5104.
- 53 N. Iyi, K. Kurashima and T. Fujita, *Chem. Mater.*, 2002, **14**, 583–589.
- 54 N. Iyi, K. Fujii, K. Okamoto and T. Sasaki, *Appl. Clay Sci.*, 2007, **35**, 218–227.